

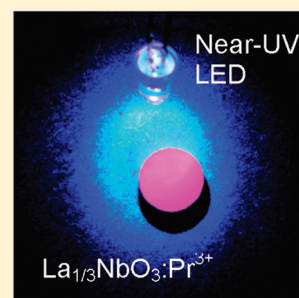
An Approach to Control of Band Gap Energy and Photoluminescence upon Band Gap Excitation in Pr^{3+} -Doped Perovskites $\text{La}_{1/3}\text{MO}_3$ ($\text{M} = \text{Nb}, \text{Ta}$): Pr^{3+}

Yoshiyuki Inaguma,* Tsunehiro Muronoi, Keiko Sano, Takeshi Tsuchiya, Yuki Mori, Tetsuhiro Katsumata,[†] and Daisuke Mori

Department of Chemistry, Faculty of Science, Gakushuin University, 1-5-1 Mejiro, Toshima-ku, Tokyo 171-8588, Japan

 Supporting Information

ABSTRACT: We synthesized polycrystalline pristine and Pr^{3+} -doped perovskites $\text{La}_{1/3}\text{MO}_3$ ($\text{M} = \text{Nb}, \text{Ta}$): Pr^{3+} and investigated their crystal structure, optical absorption, and luminescence properties. The optical band gap of $\text{La}_{1/3}\text{NbO}_3$ (3.2 eV) is smaller than that of $\text{La}_{1/3}\text{TaO}_3$ (3.9 eV), which is primarily due to the difference in electronegativity between Nb and Ta. In $\text{La}_{1/3}\text{NbO}_3$: Pr^{3+} , the red emission assigned to the $f-f$ transition of Pr^{3+} from the excited $^1\text{D}_2$ level to the ground $^3\text{H}_4$ state upon band gap photoexcitation (near-UV) was observed, whereas the $f-f$ transition of Pr^{3+} with blue-green emission from the excited $^3\text{P}_0$ level to the ground $^3\text{H}_4$ state was quenched. On the other hand, in $\text{La}_{1/3}\text{TaO}_3$: Pr^{3+} , the blue-green emission upon band gap photoexcitation was observed. Their differences in emission behavior are attributed to the energy level of the ground and excited states of $4f^2$ for Pr^{3+} , relative to the energy levels of the conduction and valence bands, and the trapped electron state, which mediates the relaxation of electron from the conduction band to the excited state of Pr^{3+} . $\text{La}_{1/3}\text{NbO}_3$: Pr^{3+} is a candidate red phosphor utilizing near-UV LED chips (e.g., $\lambda = 375$ nm) as an excitation source.



INTRODUCTION

Luminescence in lanthanide ion-doped phosphor materials is attributed to the $f-f$ or $f-d$ transition of lanthanide ion as an activator,¹ and their luminescence properties depend on host materials as well as doped lanthanide ions. In addition to ligands for doped lanthanide ions, the relative energy levels between the valence band, the conduction band of the host, and the $4f$ ground and excited states of lanthanide ion also influence the luminescence properties of the phosphor.^{2,3}

Among lanthanide ion-doped phosphor materials, Pr^{3+} -doped perovskite-type titanates ATiO_3 ($\text{A} = \text{Ca},^{4-15} \text{Sr},^{9,10,13,15-19} \text{Ba},^{9,13,20-22} (\text{La}, \text{Li}),^{23} \text{Ln}_{1/2}\text{Na}_{1/2}$ ($\text{Ln} = \text{La},^{23,24} \text{Gd}, \text{Lu}, \text{Y}^{24}$), $\text{La}_{1/2}\text{K}_{1/2}$)²³ have recently been considered attractive as red phosphor materials for a potential flat-panel display, field-emission display (FED),^{4,16,17} and electroluminescence (EL) display.²⁵ Because of recent systematic studies regarding Pr^{3+} -doped oxide phosphors with a closed-shell (electronic configuration d^0) cation M such as perovskite titanates ATiO_3 : Pr , it was proposed that their luminescence regarding the $f-f$ of Pr ion occurs via the intervalence charge transfer (IVCT) between Pr and M cations ($\text{Pr}^{3+} + \text{M}^{n+} \leftrightarrow \text{Pr}^{4+} + \text{M}^{(n-1)+}$)^{11,12,26-28} and band gap excitation processes.²⁴ Their processes are strongly influenced by the relative energy between the valence band, the conduction band of host materials, and the $4f$ ground and excited states of Pr ion. These findings imply that if we can control the energy levels of the valence and conduction bands, that is, the band gap energy of host materials, we can choose the desired excitation energy and control the luminescence properties.

Perovskite-type oxides (AMO_3) are appropriate host materials to realize this idea, because they tolerate various constituent elements and consequently change their electronic structure, that is, valence band and conduction band. The electronic structure of perovskite-type oxides is mainly ascribed to the hybridization of orbitals of the M ion and oxygen due to the three-dimensional corner-shared MO_6 octahedra.²⁹ Therefore, the selection of M ion is a key issue to determine the electronic structure in perovskite-type oxides. For example, in perovskite-type titanates $\text{A}^{2+}\text{Ti}^{4+}\text{O}_3$, the upper band-edge of the valence band primarily comprises a filled nonbonding $\text{O } 2p$ orbital, while the unoccupied conduction band originates from the antibonding π interaction between $\text{Ti } 3d$ t_{2g} and $\text{O } 2p$ orbitals.²⁹ Here, Ti^{4+} ion as M ion has a closed-shell electron configuration of $3d^0$. Consequently, the band gap energies of $\text{ATi}^{4+}\text{O}_3$ are dominated by the energy of $\text{Ti } 3d$, that is, the electronegativity of Ti ion, although there is some difference in band gap energy by A -site ion, for example, 3.56 eV for CaTiO_3 and 3.26 eV for SrTiO_3 , and 3.29 eV for $\text{La}_{1/2}\text{Na}_{1/2}\text{TiO}_3$.²⁴ This indicates that the band gap energy in AMO_3 perovskites can be controlled by the electronegativity of M ion.

In the present study, we choose two perovskite-type oxides $\text{La}_{1/3}\text{MO}_3$ ($\text{M} = \text{Nb}, \text{Ta}$)³⁰ as an approach to controlling the band gap energy. Here, Nb^{5+} and Ta^{5+} ions as M ions have the same closed-shell electron configuration of $4d^0$ and $5d^0$, respectively, but different electronegativity. In addition, these

Received: September 24, 2010

Published: May 23, 2011

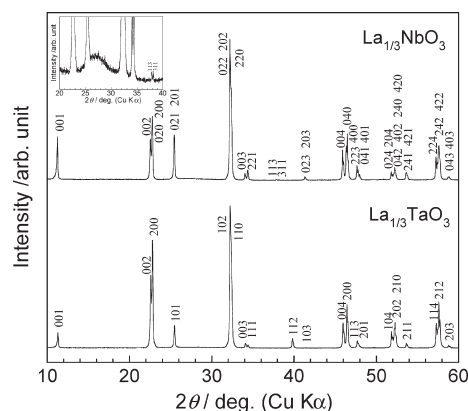


Figure 1. Powder X-ray diffraction patterns for $\text{La}_{1/3}\text{MO}_3$ ($M = \text{Nb}, \text{Ta}$). The inset shows the enlarged diffraction pattern for $\text{La}_{1/3}\text{NbO}_3$.

compounds have an advantage in that a doping ion, Pr^{3+} ion, can be substituted for La^{3+} ion without charge compensation. We report the synthesis, structure, optical band gap, and luminescence properties of Pr^{3+} -doped perovskites $\text{La}_{1/3}\text{MO}_3$ ($M = \text{Nb}, \text{Ta}$): Pr^{3+} .

EXPERIMENTAL SECTION

Polycrystalline $\text{La}_{1/3}\text{NbO}_3$ (LNO), $\text{La}_{1/3}\text{TaO}_3$ (LTO), and their Pr -doped compounds, $\text{La}_{1/3-x}\text{Pr}_x\text{MO}_3$ ($M = \text{Nb}, \text{Ta}$) (abbreviated as LNO:Pr and LTO:Pr, respectively), were synthesized by a conventional solid-state reaction at elevated temperature. The starting materials were La_2O_3 (Shin-etsu Chemicals, >99.99%), Nb_2O_5 (Mitsui Metal, >99.9%), Ta_2O_5 (Mitsui Metal, >99.9%), and $\text{Pr}(\text{NO}_3)_3$ solution. Pr nitrate solution was then prepared by dissolving Pr_6O_{11} (Rare metallic Co., >99.9%) using 3 M nitric acid. Because the reagent of La_2O_3 includes carbonates and hydrates and is sensitive to humidity, and the reagent of Pr_6O_{11} is nonstoichiometric, the metal content of each reagent was determined by chelatometry with ethylenediaminetetraacetic acid (EDTA)³¹ prior to the usage of them. The powders and solution were mixed with ethanol in an agate mortar, and then the mixture was dried in an oven at 130 °C. The dried powder was pressed into a pellet, calcined at 1100 °C for 12 h in air, and then it was ground. The calcined powder was again pressed into pellets, heated at 1300 °C for 24 h for niobates, 1550 °C for 36 h for tantalates in air, and then furnace-cooled with intermediate grindings.

The phase identification for the samples was initially carried out by the laboratory powder X-ray diffraction (XRD) using a Rigaku RINT 2100 diffractometer with a Bragg–Brentano geometry (graphite-monochromatized $\text{Cu K}\alpha$ radiation). The laboratory XRD data for Rietveld analysis were collected in the range $2\theta = 20$ – 120° in 0.02° steps at room temperature. The synchrotron XRD data for Rietveld analysis were also collected on the Debye–Scherrer diffractometer on the beamline BL-02B2 at SPring8 in Hyogo, Japan. These data were collected at 2θ of up to 75° in 0.01° steps using an imaging plate as the detector at room temperature. The wavelengths of the incident synchrotron X-ray radiation were then fixed to be 0.077268 nm for LNO and 0.051882 nm for LTO calibrated using a CeO_2 standard. The samples were then sealed in 0.2 mm diameter glass capillaries. The crystal structures of LNO and LTO were refined using the Rietveld method with the RIETAN-FP program.³² The bond valence sum (BVS) was calculated from the interatomic distances on the basis of the concept of bond valence.^{33–35} The Pr content in the sample with the nominal composition $x = 0.2\%$ was analyzed by the inductive coupled plasma (ICP) spectroscopy with a HORIBA Ultima 2 ICP optical emission spectrometer. The sample solution was then prepared as follows. A small amount of powder sample (6–10 mg) and 2–2.5 g of ammonium sulfate $(\text{NH}_4)_2\text{SO}_4$ was put into

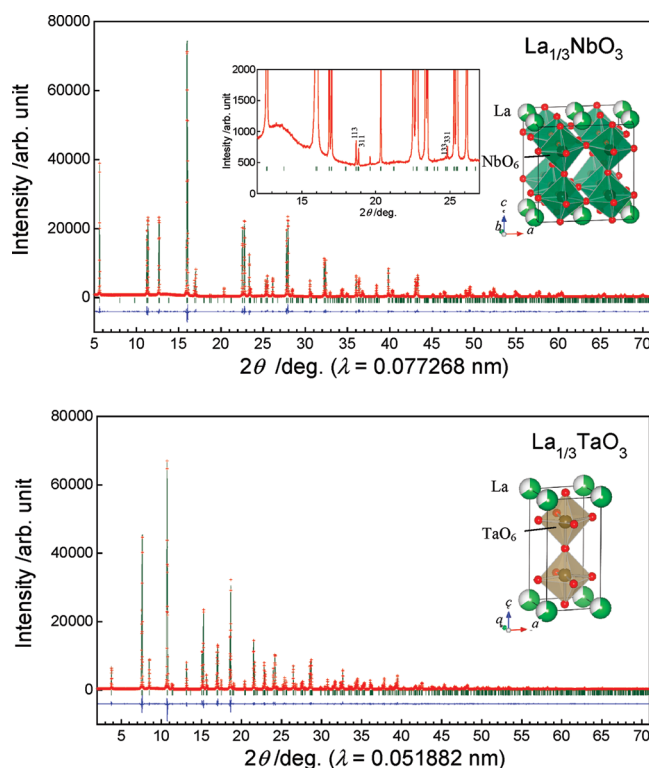


Figure 2. The observed (+) and calculated (solid line) synchrotron powder X-ray diffraction patterns, difference (solid line on the bottom) and peak positions (|) for $\text{La}_{1/3}\text{MO}_3$ ($M = \text{Nb}, \text{Ta}$) at room temperature with their refined crystal structures. The Rietveld refinements were performed using the space groups $Cmmm$ for $\text{La}_{1/3}\text{NbO}_3$ and $P4/mmm$ for $\text{La}_{1/3}\text{TaO}_3$. The inset shows the enlarged diffraction pattern for $\text{La}_{1/3}\text{NbO}_3$.

a beaker with 10 mL of concentrated sulfuric acid H_2SO_4 , which was followed by heating to dissolve the sample. After the sample was dissolved, the solution was diluted to 100 mL in a volumetric flask with deionized and distilled water.

The diffuse reflectance spectra were recorded using a JASCO V-550 ultraviolet and visible spectrophotometer. Photoluminescence and excitation spectra were recorded using a JASCO FP-6500 spectrofluorometer at room temperature. Light from a 150 W xenon lamp was used as an excitation source. Photoluminescence spectra were recorded from 370 to 850 nm with an excited wavelength of 220–550 nm, and excitation spectra were recorded from 220 to 550 nm with respect to the wavelength of the luminescence peak. The instrument response function has been measured using a halogen standard lamp, and Rhodamine B in ethylene glycol (8 g/L) with a quantum efficiency of 100%.³⁶ The correction file normalizes the emission and excitation spectra.

RESULTS AND DISCUSSION

Crystal Structure of $\text{La}_{1/3}\text{MO}_3$ ($M = \text{Nb}, \text{Ta}$). Figure 1 shows the powder laboratory XRD patterns with $\text{Cu K}\alpha$ radiation for LNO and LTO. The observed and calculated synchrotron XRD patterns from the Rietveld analysis for both compounds are shown in Figure 2. As previously reported, LNO^{37–39} and LTO^{30,40} crystallize as orthorhombic and tetragonal perovskites, respectively. Both compounds exhibit superstructural peaks corresponding to the alternative ordered arrangement of La and A-site vacancies along the c -axis, which doubles the lattice parameter along the c -axis, as shown in the inset of Figure 2. Here, the crystal structures were drawn with the computer program VESTA.⁴¹

Table 1. Refined Structural Parameters for $\text{La}_{1/3}\text{NbO}_3$ Using the Synchrotron X-ray Diffraction Data^a

	Wyckoff site	<i>g</i>	<i>x</i>	<i>y</i>	<i>z</i>	<i>B</i> /Å ²
La	4i	2/3	0	0.2479(3)	0	0.666(9)
Nb	8o	1	0.2501(3)	0	0.26103(4)	1.183(7)
O1	4g	1	0.2271(6)	0	0	1.27(10)
O2	4h	1	0.2703 (9)	0	1/2	0.91(9)
O3	4k	1	0	0	0.2542(7)	0.28(10)
O4	4l	1	0	1/2	0.2061(8)	1.65(14)
O5	8m	1	1/4	1/4	0.2329(4)	0.87(5)

^aSpace group: *Cmmm* (No. 65), *Z* = 8. Lattice parameters (orthorhombic): *a* = 0.78240(1) nm, *b* = 0.78432(1) nm, *c* = 0.79165(1) nm. *R*_{wp} = 4.27%, *R*_p = 3.14%, *R*_e = 3.29%, *S* = 1.30, *R*_i = 3.00%, *R*_f = 3.61%. Uncertainties are shown in parentheses, following the last significant figures to which they are attributed.

In addition, as shown in the insets of Figure 1, LNO exhibits the weak superstructural peaks with indices of 311 and 113. The other superstructural peaks with indices of odd odd odd such as 133, 331 at higher angle were also detected in the synchrotron X-ray diffraction pattern of $\text{La}_{1/3}\text{NbO}_3$ as shown in the inset of Figure 2, although it was too weak to detect them apparently in the laboratory X-ray diffraction pattern. On the other hand, the intensities of peaks with indices of 131 and 313 are relatively weaker. This result indicates that the antiphase tilting of corner-shared NbO_6 octahedra occurs along the *b*-axis (Glazer notation:^{42,43} $a^0b^-c^0$) when the cell dimensions have the following relation $a < b < c$, which also doubles the lattice parameter along the *a*- and *b*-axes.⁴⁴ On the other hand, LTO exhibits no similar superstructural lines, indicating no tilting of corner-shared TaO_6 octahedra at room temperature, although the tilting of TaO_6 octahedral appears at lower than about 220 K.⁴⁵ Consequently, LNO possesses a unit cell of $\sim 2a_p \times \sim 2a_p \times \sim 2a_p$ with a space group *Cmmm*, whereas LTO has a unit cell of $\sim a_p \times \sim a_p \times \sim 2a_p$ with a space group *P4/mmm*. Here, *a_p* denotes the basic perovskite unit cell. Furthermore, in the XRD pattern of LNO (see the insets of Figure 1 and 2), a very broad peak-like background can be observed in the vicinity of $2\theta = 27^\circ$ for XRD pattern with Cu K α radiation and $2\theta = 13.5^\circ$ for synchrotron XRD pattern, which is slightly smaller than the 2θ corresponding to the 112 peak. A similar phenomenon can be seen in a synchrotron XRD pattern of LNO reported by Kennedy et al.³⁹ This may be related to the short-range order of La ion or the microdomain structure. The refined structural parameters from the Rietveld analysis for both compounds using the synchrotron XRD data are summarized in Tables 1 and 2. For comparison, in the Supporting Information, the observed and calculated laboratory XRD patterns from the Rietveld analysis are shown in Figure S1 and S2, and the refined structural parameters using the laboratory XRD data and synchrotron XRD data are summarized (see Tables S1 and S2). The results are consistent with those of previous reports,^{30,37–40} although there are differences between some parameters such as lattice parameters. The selected interatomic distances and angles for LNO and LTO refined using the synchrotron XRD data were summarized in Table 3. For comparison, in the Supporting Information, the refined selected interatomic distances and angles using the laboratory XRD data and synchrotron XRD data are summarized (see Tables S3). As seen in Table 3, the average interatomic distances M–O, La–O, and La–M are almost the same for LNO

Table 2. Structural Parameters for $\text{La}_{1/3}\text{TaO}_3$ Using the Synchrotron X-ray Diffraction Data^a

	Wyckoff site	<i>g</i>	<i>x</i>	<i>y</i>	<i>z</i>	<i>B</i> /Å ²
La	1a	2/3	0	0	0	0.70(1)
Ta	2h	1	1/2	1/2	0.25984(4)	0.754(5)
O1	1c	1	1/2	1/2	0	1.41(13)
O2	1d	1	1/2	1/2	1/2	1.69(14)
O3	4i	1	0	1/2	0.2320(4)	0.99(5)

^aSpace group: *P4/mmm* (No. 123), *Z* = 2. Lattice parameters (tetragonal): *a* = 0.39186(1) nm, *c* = 0.79149(1) nm. *R*_{wp} = 5.28%, *R*_p = 3.94%, *R*_e = 3.78%, *S* = 1.40, *R*_i = 2.37%, *R*_f = 2.69%. Uncertainties are shown in parentheses, following the last significant figures to which they are attributed.

and LTO. The distortion of MO_6 estimated by the equation,³³

$$\Delta = \frac{1}{6} \sum_{i=1}^6 \left\{ \left(\frac{d_i - d_{av}}{d_{av}} \right)^2 \right\}$$

$\Delta = 7.1 \times 10^{-4}$ for NbO_6 in LNO is greater than $\Delta = 5.2 \times 10^{-4}$ for TaO_6 in LTO. Here, d_i and d_{av} denote the individual interatomic distance of M–O and the average distance, respectively. In addition, the bond angle of Nb–O–Nb in LNO deviates from 180° due to the tilting of NbO_6 octahedra. The calculated bond valence sums for La and M (M = Nb, Ta) ions are also listed in Table 3. The values of BVS are consistent with trivalent La ion and pentavalent Nb and Ta ions. Slightly smaller BVS of La for both compounds indicates that the average interatomic distances of La–O are greater than usual, that is, under-bonded. On the other hand, when we examined each bond distance of La–O, the bond distances of La–O1, La–O4, La–O5 for LNO, and La–O3 for LTO are relatively shorter, which is attributed to the alternative ordering of vacancies at the A-site along the *c*-axis. Here, O1, O4, O5 for LNO and O3 for LTO are located between the La layer and vacant layer. The alternative ordering causes the shift of Nb and Ta ion toward the vacant layer of A-site and the shift of their oxygen ions toward the La layer, resulting in the shorter bond distance of La–O. Because the Pr ions substitute for La site in Pr-doped compounds, this structural characteristic anticipates that electron transfer between Pr and O should be easier.

Optical Band Gap of $\text{La}_{1/3}\text{MO}_3$ (M = Nb, Ta). Figure 3 shows the diffuse reflectance spectra of LNO and LTO. The absorption spectra are shown in the inset of Figure 3. Here, the diffuse reflectance data were transformed into absorbance with the Kubelka–Munk function.⁴⁶ As seen in Figure 3, the energy of the optical absorption edge of LNO is lower than that of LTO. The estimated band gap energies are 3.22 eV ($\lambda = 385$ nm) and 3.87 eV ($\lambda = 320$ nm) for LNO and LTO, respectively. The band gap energy of 3.22 eV for LNO is less than 3.56 eV for CaTiO_3 and 3.26 eV for SrTiO_3 . According to the molecular orbital approach,²⁹ the band-edge of the valence band primarily comprises a filled nonbonding O 2p orbital, while the unoccupied conduction band originates from the antibonding π interaction between Nb (Ta) 4d (5d) t_{2g} and O 2p orbitals. The difference in band gap energy is therefore primarily due to differences in (i) electronegativity, χ of M ion, Nb and Ta ions, which determines the energy level of the d orbital of M ion, and (ii) the distortion and tilting of MO_6 octahedra, which determines the conduction bandwidth associated with antibonding interaction between the

Table 3. Selected Interatomic Distances (nm), Bond Angles (deg), the Distortion of MO₆ Octahedron Δ , and Calculated Bond Valence Sum (BVS) of Cations at Room Temperature for La_{1/3}NbO₃ and La_{1/3}TaO₃ Refined Using the Synchrotron X-ray Diffraction Data

	La _{1/3} NbO ₃	La _{1/3} TaO ₃
Distance		
M–O1	0.20742(7) × 1	0.20566(3) × 1
M–O2	0.18984(7) × 1	0.19009(3) × 1
M–O3	0.19572(3) × 1	0.19717(3) × 4
M–O4	0.20033(3) × 1	
M–O5	0.19734(4) × 2	
average M–O(<i>d</i> _{av})	0.1980	0.1974
$\Delta = 1/6\{(d_{M-O} - d_{av})/d_{av}\}^2$	7.1×10^{-4}	5.2×10^{-4}
La–O1	0.2642(5) × 2	0.27709(1) × 4
	0.2910(5) × 2	
La–O3	0.2798(4) × 2	0.2685(2) × 8
La–O4	0.2563(5) × 2	
La–O5	0.2688(2) × 4	
average La–O	0.2715	0.2714
La–M	0.3446(2) × 4	0.34507(2) × 8
	0.3465(2) × 4	
average La–M	0.3456	0.3451
Bond Angle		
M–O1–M	170.1(4)	180
M–O2–M	170.4(5)	180
M–O3–M	176.8(3)	167.2(2)
M–O4–M	154.9(4)	
M–O5–M	167.0(2)	
BVS		
atom (assumed valence)	BVS (deviation from assumed valence)	BVS (deviation from assumed valence)
La (+3)	2.89 (–4%)	2.79 (–7%)
M (+5)	5.03 (+1%)	5.22 (+4%)

nd orbital of M ion and the O 2p orbital.²⁹ Jørgensen⁴⁷ has derived the optical electronegativity χ_{opt} from electron transfer spectra of octahedral hexahalide complexes. The value of χ_{opt} for Nb(V) is 1.85, and the value of χ_{opt} for Ta(V) is 1.8. According to the difference in electronegativity, the energy difference between the Nb 4d orbital and the O 2p orbital is smaller than that between the Ta 5d orbital and the O 2p orbital, resulting in a smaller band gap for LNO than that of LTO. Next, we consider the effect of the distortion and tilting of MO₆ on the band gap energy E_g . The distortion and tilting of MO₆ eliminate the antibonding π interaction between the M *nd* t_{2g} orbital and the O 2p orbital, resulting in a decrease in the width of conduction band, that is, the increase in band gap. As mentioned in the previous section, because the degree of distortion and tilting of MO₆ in LNO is greater than those in LTO, the effect of the distortion and tilting of MO₆ octahedra in LNO on the increase in band gap is greater than that in LTO. Therefore, the smaller optical band gap of LNO than that of LTO is primarily due to the difference in electronegativity between Nb and Ta.

Luminescence Properties of Pr-Doped La_{1/3}MO₃ (M = Nb, Ta):Pr³⁺. According to the ICP analysis, it was confirmed that the actual Pr content in the sample is close to the nominal one. The Pr content $x = 0.188 \pm 0.008\%$ for LNO:Pr ($x = 0.2\%$) and $x = 0.199 \pm 0.002$ for LTO:Pr ($x = 0.2\%$). Figure 4 shows the emission (excitation wavelength: $\lambda_{\text{ex}} = 360$ nm) and excitation

(emission wavelength: $\lambda_{\text{em}} = 608$ nm) spectra of LNO:Pr ($x = 0.2\%$) with the diffuse reflectance of pristine LNO. As shown in Figure 4, LNO:Pr shows a red emission, corresponding to the f–f transition of Pr³⁺ (¹D₂ to ³H₄), and several emissions in the near-infrared-red region, corresponding to the transitions of ¹D₂ to ³H₅ ($\lambda \approx 700$ nm), and ¹D₂ to ³H₆ ($\lambda \approx 820$ nm).¹ However, the green-blue emission corresponding to the f–f transition of ³P₀ to ³H₄ was then quenched. These behaviors are the same as those of Pr-doped perovskite titanates. The peak of the excitation spectrum is located in the vicinity of the absorption edge of LNO, indicating that the emission can partly be attributed to the band gap excitation (Figure 5a). In CaTiO₃:Pr and other Pr³⁺-doped compounds,^{11,12,15,24,26,27} the shoulder band corresponding to the transition from the ground state ³H₄ of Pr³⁺ to the bottom of the conduction band, that is, IVCT excitation (Figure 5b), has apparently been observed on the lower energy side of the excitation peak. For LNO:Pr, the distinct shoulder band was not observed in the excitation spectrum. However, LNO:Pr shows the excitation peak with the low-energy halfway point coinciding with the halfway point of the absorption. This suggests the possibility that the contribution of the IVCT excitation on the lower energy side overlaps with that of the band gap excitation. Here, because the bottom of conduction band is primarily originated from the antibonding contribution between M *nd* t_{2g} and oxygen 2p atomic orbital, the IVCT model

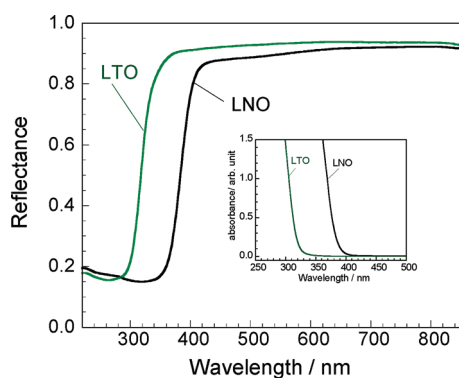


Figure 3. Diffuse reflectance spectra of $\text{La}_{1/3}\text{NbO}_3$ (LNO) and $\text{La}_{1/3}\text{TaO}_3$ (LTO). The inset is their absorption spectra.

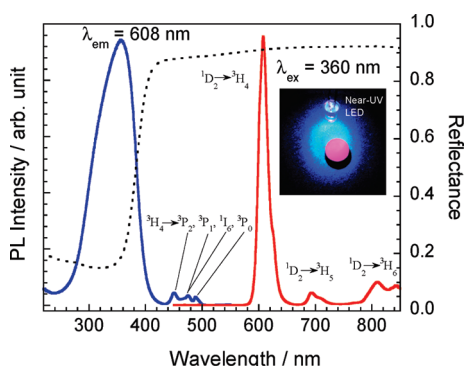


Figure 4. Emission and excitation spectra of $\text{La}_{1/3}\text{NbO}_3\text{:Pr}^{3+}$ 0.2%. Dotted line indicates diffuse reflectance spectrum of $\text{La}_{1/3}\text{NbO}_3$. The inset shows the photograph of $\text{La}_{1/3}\text{NbO}_3\text{:Pr}^{3+}$ 0.2% upon photoexcitation using a near-UV LED with a peak wavelength of 375 nm.

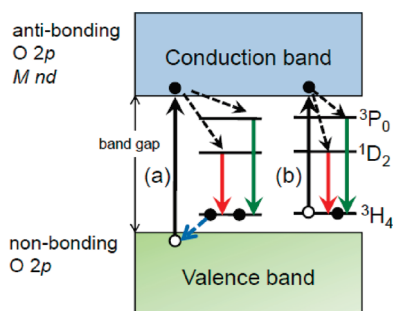


Figure 5. Schematics of the relation between the band structure and the energy levels of 4f state of Pr^{3+} , emission upon the band gap excitation (a) and the IVCT excitation (b).

of $\text{Pr}^{3+}/\text{M}^{n+} \rightarrow \text{Pr}^{4+}/\text{M}^{(n-1)+}$ proposed by Boutinaud et al.^{11,12,26,27} is consistent with the scheme derived by the approach in terms of the electronic structure shown in Figure 5b. The maximum emission intensity was observed when the Pr content x was 0.15% (see Supporting Information, Figure S3). On the basis of the emission spectrum of LNO:Pr 0.2% shown in Figure 4, the Commission Internationale de l'Eclairage (CIE) chromaticity coordinates were calculated to be (0.654, 0.342), which is close to the National Television Standard Committee red (0.67, 0.33). Furthermore, the inset of Figure 4 shows the photograph of LNO:Pr 0.2% upon photoexcitation using a NICHIA NSPU510CS UV LED

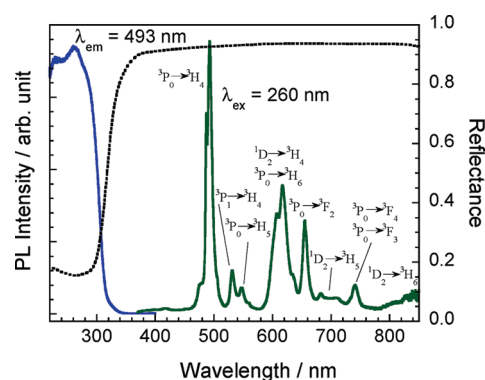


Figure 6. Emission and excitation spectra of $\text{La}_{1/3}\text{TaO}_3\text{:Pr}^{3+}$ 0.2%. Dotted line indicates diffuse reflectance spectrum of $\text{La}_{1/3}\text{TaO}_3$.

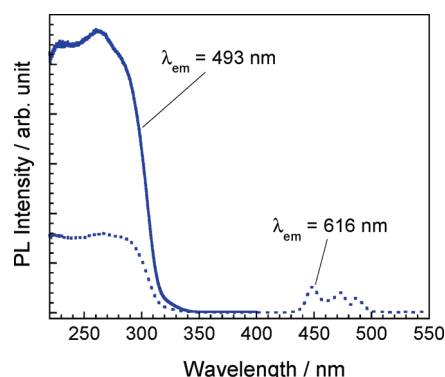


Figure 7. Excitation spectra for blue-green ($\lambda_{\text{em}} = 493$ nm) and red ($\lambda_{\text{em}} = 616$ nm) emissions of $\text{La}_{1/3}\text{TaO}_3\text{:Pr}^{3+}$ 0.2%.

with a peak wavelength of 375 nm. The finding of red emission indicates that LNO:Pr is a candidate red phosphor utilizing near-UV LED chips as an excitation source.

The luminescence properties of LTO:Pr are different from those of LNO:Pr. Figure 6 shows the emission (excitation wavelength: $\lambda_{\text{ex}} = 260$ nm) and excitation (emission wavelength: $\lambda_{\text{em}} = 493$ nm) spectra of LTO:Pr ($x = 0.2\%$) with diffuse reflectance of pristine LTO. LTO:Pr shows a blue-green emission with a wavelength of 490 nm, corresponding to the f–f transition of Pr^{3+} ($^3\text{P}_0$ to $^3\text{H}_4$), red emission corresponding to the f–f transition of Pr^{3+} ($^1\text{D}_2$ to $^3\text{H}_4$ and $^3\text{P}_0$ to $^3\text{H}_6$), and several emissions in the near-infrared-red region, corresponding to the transitions of $^1\text{D}_2$ to $^3\text{H}_5$ ($\lambda \approx 700$ nm), $^1\text{D}_2$ to $^3\text{H}_6$ ($\lambda \approx 820$ nm).¹ The excitation spectrum of LTO:Pr exhibits different features from that of LNO:Pr. A peak in the longer wavelength region of the excitation spectrum corresponds to the absorption edge of LTO, indicating that part of the emissions can be attributed to the band gap excitation the same as LNO:Pr. Another peak in the shorter wavelength region of the excitation spectrum can also be observed. This peak may correspond to the f–d transition of Pr^{3+} . On the other hand, the distinct shoulder band on the longer wavelength side in the excitation spectrum corresponding to IVCT excitation was not observed for LTO:Pr. As shown in Figure 7, the excitation spectra with regard to green-blue emissions ($\lambda = 493$ nm) and red emissions ($\lambda = 616$ nm) exhibit the same profiles, indicating that both emissions occur via the same excitation process. The maximum emission intensity was observed when the Pr content x was 1.0% (see Supporting

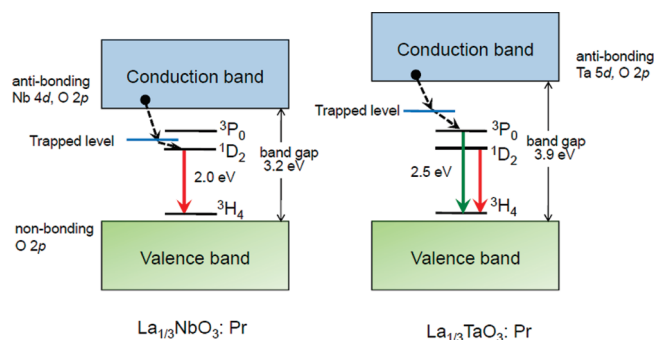


Figure 8. Schematics of the relation between the band structure and the energy levels of 4f state of Pr^{3+} , the trapped state, and the relaxation from the conduction band to the excited level via the trapped state in $\text{La}_{1/3}\text{NbO}_3:\text{Pr}^{3+}$ and $\text{La}_{1/3}\text{TaO}_3:\text{Pr}^{3+}$.

Information, Figure S4). The Pr content for LTO:Pr, in which the maximum intensity was observed, was greater than that for LNO:Pr. The possible explanations for this result are as follows. In LNO:Pr, the site symmetry of Pr^{3+} is C_{2v} ($m2m$) without an inversion center, when Pr^{3+} ions reside in the La site (4i site). On the other hand, in LTO:Pr, the site symmetry of Pr^{3+} is D_{4h} ($4/mmm$) with an inversion center. The transition from the ground state $^3\text{H}_4$ to the excited state of Pr^{3+} is therefore allowed in LNO:Pr, while it is forbidden in LTO:Pr in terms of site symmetry. Because the concentration quenching of emission is primarily due to the cross-relaxation, the concentration quenching strongly depends on the probability for the absorption of emission. The higher transition probability in LNO:Pr than in LTO:Pr promotes the cross-relaxation, resulting in the quenching in the lower Pr^{3+} concentration.

Finally, we discuss the difference in the luminescence properties between LNO:Pr and LTO:Pr, that is, the quenching of the $^3\text{P}_0$ to $^3\text{H}_4$ emission of Pr^{3+} in LNO:Pr, while the observation of the emission in LTO:Pr, in terms of the relaxation of the excited electron at the conduction band to the excited state of Pr^{3+} . Boutinaud et al.^{11,12,26,27} proposed that the relaxation to the excited state of Pr^{3+} can be explained by using the IVCT relaxation model. The electron at the conduction band relaxes to the excited state of Pr^{3+} via the IVCT state. The energy position of IVCT state relative to the excited states, $^3\text{P}_0$ and $^1\text{D}_2$ of Pr^{3+} , therefore determines emission colors, that is, whether the quenching of emission from $^3\text{P}_0$ level occurs or not. On the other hand, because the IVCT state is a virtual state, it is difficult to define the meaning concretely. Gryk et al.^{48,49} proposed the alternate model of a Pr^{3+} trapped exciton with a hole localized at Pr^{3+} ion (Pr^{4+}) and an electron partly bounded by the Coulomb potential of the hole. However, the relation between the energy level of Pr^{3+} trapped exciton and the electronic structure of host lattice was not discussed. We then propose the presence of an electron-trapped state, which is located below the electronic state of the d orbital of M ion and mediates between the conduction band and the excited state of Pr^{3+} instead of the IVCT relaxation state and Pr^{3+} trapped exciton state. The trapped state originates from intrinsic defects such as the oxygen vacancies in the host lattice. When the state originates from oxygen vacancies, it is localized on the d orbital of the adjacent M ion.⁵⁰ As mentioned above, because the conduction band has strong metal d orbital characters, originating from the antibonding metal–oxygen interaction, the energy level of the electron-trapped state changes with

the energy level of the conduction band. On the basis of the results, the schematic of the relaxation of electron from the conduction band to the excited state of Pr^{3+} via an electron-trapped state for LNO:Pr and LTO:Pr is shown in Figure 8. The trapped state in LNO:Pr is located between $^3\text{P}_0$ and $^1\text{D}_2$ levels of Pr^{3+} , resulting in the electron transfer to the $^2\text{D}_1$ level and the emission from $^2\text{D}_1$ level, that is, the quenching of the emission from $^3\text{P}_0$ level. The trapped state in LTO:Pr is located above the $^3\text{P}_0$ level, resulting in the electron transfer to the $^3\text{P}_0$ level and the emission from $^3\text{P}_0$ level. Furthermore, the energy level of ground state of Pr^{3+} , $^3\text{H}_4$ is located in the vicinity of that of the valence band. Consequently, the band gap energy is a predominant factor in determining the emission colors in addition to the excitation energies in Pr-doped perovskite-type oxides.

CONCLUSION

We chose two perovskite-type oxides $\text{La}_{1/3}\text{MO}_3$ ($\text{M} = \text{Nb}, \text{Ta}$) as an approach to controlling the band gap energy and elucidated the luminescence properties of Pr^{3+} -doped $\text{La}_{1/3}\text{MO}_3$ ($\text{M} = \text{Nb}, \text{Ta}$): Pr^{3+} . It was then found that the selection of M ion (Nb and Ta) with different electronegativities changes the band gap energies of host perovskite-type oxides, $\text{La}_{1/3}\text{MO}_3$ ($\text{M} = \text{Nb}, \text{Ta}$), which strongly influences the luminescence properties such as the emission colors upon band gap photoexcitation in addition to changing the excitation energies in Pr-doped perovskites, $\text{La}_{1/3}\text{MO}_3$ ($\text{M} = \text{Nb}, \text{Ta}$): Pr^{3+} . We proposed the electron trapped state with d orbital characters, originating from defects in the host lattice, mediates the relaxation of electron from the conduction band to the excited states of Pr^{3+} and explained the differences in luminescence properties between $\text{La}_{1/3}\text{NbO}_3:\text{Pr}^{3+}$ and $\text{La}_{1/3}\text{TaO}_3:\text{Pr}^{3+}$. The findings in this study provided an aspect of luminescence mechanism based on the band gap excitation in Pr^{3+} -doped perovskites and a strategy for designing phosphor materials with desired excitation energies. $\text{La}_{1/3}\text{NbO}_3:\text{Pr}^{3+}$ is then a candidate red phosphor utilizing near-UV LED chips as an excitation source.

ASSOCIATED CONTENT

S Supporting Information. Laboratory powder X-ray diffraction patterns and the results of Rietveld refinement for $\text{La}_{1/3}\text{MO}_3$ ($\text{M} = \text{Nb}, \text{Ta}$). Refined structural parameters for $\text{La}_{1/3}\text{MO}_3$ ($\text{M} = \text{Nb}, \text{Ta}$) using laboratory X-ray diffraction data. Emission intensities versus the Pr content for $\text{La}_{1/3}\text{MO}_3$ ($\text{M} = \text{Nb}, \text{Ta}$): Pr^{3+} . This material is available free of charge via the Internet at <http://pubs.acs.org>.

AUTHOR INFORMATION

Corresponding Author

*E-mail: yoshiyuki.inaguma@gakushuin.ac.jp.

Present Addresses

[†]Department of Chemistry, School of Science, Tokai University, 4-1-1 Kitakaname, Hiratsuka, Kanagawa 259-1292, Japan.

ACKNOWLEDGMENT

We thank Dr. H. Takashima for his help in the calculation of the CIE chromaticity coordinates, and Mr. A. Aimi and Ms. K. Tanaka for the experimental support of synchrotron XRD measurement. We are also grateful to the reviewers for their useful advice and helpful comments. The synchrotron XRD measurements were

carried out under the Priority Nanotechnology Support Program administered by the Japan Synchrotron Radiation Research Institute (JASRI) (Proposal No. 2010A1669). This work was supported by a Grant-in-Aid for Scientific Research (No. 17560598) of JSPS and the “High-Technology Research Center Project” of the Ministry of Education, Culture, Sports, Science and Technology of Japan.

■ REFERENCES

- (1) Dieke, G. H.; Crosswhite, H. M. *Appl. Opt.* **1963**, *2*, 675–686.
- (2) Dorenbos, P. J. *Phys.: Condens. Matter* **2003**, *15*, 8417–8434.
- (3) Krumpel, A. H.; Kolk, E. v. d.; Cavalli, E.; Boutinaud, P.; Bettinelli, M.; Dorenbos, P. J. *Phys.: Condens. Matter* **2009**, *21*, 115503.
- (4) Cho, S. H.; Yoo, J. S.; Lee, J. D. *J. Electrochem. Soc.* **1996**, *143*, L231–L234.
- (5) Diallo, P. T.; Boutinaud, P.; Mahiou, R.; Cousseins, J. C. *Phys. Status Solidi A* **1997**, *160*, 255–263.
- (6) Okamoto, S.; Yamamoto, H. *Appl. Phys. Lett.* **2001**, *78*, 655–657.
- (7) Diallo, P. T.; Jeanlouis, K.; Boutinaud, P.; Mahiou, R.; Cousseins, J. C. *J. Alloys Compd.* **2001**, *323–324*, 218–222.
- (8) Pan, Y.; Su, Q.; Xu, H.; Chen, T.; Ge, W.; Yang, C.; Wu, M. *J. Solid State Chem.* **2003**, *174*, 69–73.
- (9) Okamoto, S.; Yamamoto, H. *J. Lumin.* **2003**, *102–103*, 586–589.
- (10) Jia, W.; Xu, W.; Rivera, I.; Perez, A.; Fernandez, F. *Solid State Commun.* **2003**, *126*, 153–157.
- (11) Pinel, E.; Boutinaud, P.; Mahiou, R. *J. Alloys Compd.* **2004**, *380*, 225–229.
- (12) Boutinaud, P.; Pinel, E.; Dubois, M.; Vink, A. P.; Mahiou, R. *J. Lumin.* **2005**, *111*, 69–80.
- (13) Kyömen, T.; Sakamoto, R.; Sakamoto, N.; Kunugi, S.; Itoh, M. *Chem. Mater.* **2005**, *17*, 3200–3204.
- (14) Deren, P. J.; Pazik, R.; Strek, W.; Boutinaud, P.; Mahiou, R. *J. Alloys Compd.* **2008**, *451*, 595–599.
- (15) Boutinaud, P.; Sarakha, L.; Cavalli, E.; Bettinelli, M.; Dorenbos, P.; Mahiou, R. *J. Phys. D: Appl. Phys.* **2009**, *42*, 045106.
- (16) Toki, H.; Sato, Y.; Tamura, K.; Kataoka, F.; Itoh, S. *Proceedings of Third International Display workshop*, 1996; Vol. 2, pp 519–520.
- (17) Itoh, S.; Toki, H.; Tamura, K.; Kataoka, F. *Jpn. J. Appl. Phys.* **1999**, *38*, 6387–6391.
- (18) Yamamoto, H.; Okamoto, S.; Kobayashi, H. *J. Lumin.* **2002**, *100*, 325–332.
- (19) Inaguma, Y.; Nagasawa, D.; Katsumata, T. *Jpn. J. Appl. Phys.* **2005**, *44*, 761–764.
- (20) Yamamoto, H.; Okamoto, S. *Displays* **2000**, *21*, 93–98.
- (21) Okamoto, S.; Yamamoto, H. *J. Appl. Phys.* **2002**, *91*, 5492–5494.
- (22) Li, J.; Wu, Y. J.; Kuwabara, M. *Jpn. J. Appl. Phys., Part 2* **2005**, *44*, L708–L710.
- (23) Hyeon, K. A.; Byeon, S. H.; Park, J. C.; Kim, D. K.; Suh, K. S. *Solid State Commun.* **2000**, *115*, 99–104.
- (24) Inaguma, Y.; Tsuchiya, T.; Katsumata, T. *J. Solid State Chem.* **2007**, *180*, 1678–1685.
- (25) Takashima, H.; Shimada, K.; Miura, N.; Katsumata, T.; Inaguma, Y.; Ueda, K.; Itoh, M. *Adv. Mater.* **2009**, *21*, 3699–3702.
- (26) Boutinaud, P.; Pinel, E.; Oubaha, M.; Mahiou, R.; Cavalli, E.; Bettinelli, M. *Opt. Mater.* **2005**, *28*, 9–13.
- (27) Boutinaud, P.; Mahiou, R.; Cavalli, E.; Bettinelli, M. *Chem. Phys. Lett.* **2006**, *418*, 185–188.
- (28) Boutinaud, P.; Sarakha, L.; Mahiou, R.; Dorenbos, P.; Inaguma, Y. *J. Lumin.* **2010**, *130*, 1725–1729.
- (29) Eng, H. W.; Barnes, P. W.; Auer, B. M.; Woodward, P. M. *J. Solid State Chem.* **2003**, *175*, 94–109.
- (30) Iyer, P. N.; Smith, A. J. *Acta Crystallogr.* **1967**, *23*, 740–746.
- (31) Christian, G. D. *Analytical Chemistry*, 6th ed.; Wiley: New York, 2004.
- (32) Izumi, F.; Momma, K. *Solid State Phenomena* **2007**, *130*, 15–20.
- (33) Brown, I. D.; Shannon, R. D. *Acta Crystallogr., Sect. A* **1973**, *29*, 266–282.
- (34) Altermatt, D.; Brown, I. D. *Acta Crystallogr., Sect. B* **1985**, *41*, 240–244.
- (35) Brese, N. E.; O’Keeffe, M. *Acta Crystallogr., Sect. B* **1991**, *47*, 192–197.
- (36) Melhuish, W. H. *J. Opt. Soc. Am.* **1962**, *52*, 1256–1258.
- (37) Dilanian, R. A.; Yamamoto, A.; Izumi, F.; Kamiyama, T. *Mol. Cryst. Liq. Cryst. Sci. Technol., Sect. A* **2000**, *341*, 225–230.
- (38) Howard, C. J.; Zhang, Z. *Acta Crystallogr., Sect. B* **2004**, *60*, 249–251.
- (39) Kennedy, B. J.; Howard, C. J.; Kubota, Y.; Kato, K. *J. Solid State Chem.* **2004**, *177*, 4552–4556.
- (40) Zhou, Q.; Saines, P. J.; Sharma, N.; Ting, J.; Kennedy, B. J.; Zhang, Z.; Withers, R. L.; Wallwork, K. S. *Chem. Mater.* **2008**, *20*, 6666–6676.
- (41) Momma, K.; Izumi, F. *J. Appl. Crystallogr.* **2008**, *41*, 653–658.
- (42) Glazer, A. *Acta Crystallogr., Sect. B* **1972**, *28*, 3384–3392.
- (43) Glazer, A. *Acta Crystallogr., Sect. A* **1975**, *31*, 756–762.
- (44) Inaguma, Y.; Katsumata, T.; Itoh, M.; Morii, Y. *J. Solid State Chem.* **2002**, *166*, 67–72.
- (45) Salak, A. N.; Vyshatko, N. P.; Khalyavin, D. D.; Prokhnenko, O.; Ferreira, V. M. *Appl. Phys. Lett.* **2008**, *93*, 162903–3.
- (46) Kubelka, P.; Munk, F. Z. *Tech. Phys.* **1931**, *12*, 593–601.
- (47) Jørgensen, C. K. *Prog. Inorg. Chem.* **1970**, *12*, 101.
- (48) Gryk, W.; Dyl, D.; Ryba-Romanowski, W.; Grinberg, M. *J. Phys.: Condens. Matter* **2005**, *17*, 5381–5395.
- (49) Gryk, W.; Dujardin, C.; Joubert, M. F.; Ryba-Romanowski, W.; Malinowski, M.; Grinberg, M. *J. Phys.: Condens. Matter* **2006**, *18*, 117–125.
- (50) Robertson, J.; Xiong, K.; Clark, S. J. *Thin Solid Films* **2006**, *496*, 1–7.

■ NOTE ADDED AFTER ASAP PUBLICATION

The equation below Table 2 was incorrect in the version published ASAP May 23, 2011; the correct version reposted May 25, 2011.